J. Fluid Mech. (1999), *vol.* 392, *pp.* 129–153. Printed in the United Kingdom

Experimental and numerical analysis of circular pulse jets

By R. ISHII[1], H. FUJIMOTO[1], N. HATTA[1] AND Y. UMEDA[2]

[1]Department of Energy Science and Technology, Graduate School of Energy Science, Kyoto University, Kyoto 606-8501, Japan
[2]Department of Aeronautics and Astronautics, Graduate School of Engineering, Kyoto University, Kyoto 606-8501, Japan

(Received 29 May 1998 and in revised form 27 February 1999)

Unsteady circular jets are treated experimentally and numerically. The time evolution of circular pulse jets is investigated systematically for a wide range of jet strength, with the focus on the jet evolution, in particular the formation processes of Mach disks in the middle stage and of shock-cell structures in the later stage. It is shown that unsteady second shocks are realized for all sonic underexpanded jets and they either breed conical shocks for lower pressure ratios or truncated cones (Mach disk and reflected shock) for higher pressure ratios. The vortex ring produced near the nozzle lip plays an important role in the formation of the shock-cell structure. In particular, interactions between the vortex ring and the Mach disk connected with a strong second shock affect remarkably the formation process of the first shock cell. Different formation processes of the first cell structure are found. It is also made clear that the Kelvin–Helmholtz instability along slip surfaces originating from the triple point at the outer edge of the Mach disk is responsible for the generation of large second vortices which entrain the first vortex. This results in strong mixing between the primary jet and surrounding gas for higher pressure ratios. Numerical simulations with a TVD-scheme for the Euler equations are also performed and the numerical results are compared with the experimental ones to understand and predict the flow characteristics of the pulse jets.

1. Introduction

Supersonic jets have been used in many research fields and are also realized in many practical applications. Laminar supersonic jets are used in aerodynamic levitation flow reactors. In kraft recovery boilers, supersonic jets are applied as sootblowers to remove the fireside deposit. They are also used for gas atomization of melt metal to produce small metal powders and for oxygen-fuel flame spraying. At the lift-off of a rocket, unsteady supersonic jets are exhausted from nozzles just after the ignition, and in the operation of an air bag in a car an unsteady supersonic jet is applied. Furthermore, recently, it has been recognized that pulsed supersonic jets provide effective means to control the chemical energy release in variety of combustion systems – as utilized in advanced concepts for internal combustion engines (Oppenheim & Maxon 1991; Kuhl *et al.* 1997).

So far, the unsteady jet has been investigated mainly experimentally due to its strong nonlinearity (Elder & De Haas 1952; Golub 1994; Payman & Shepherd 1946; Schmidt & Shear 1975). The first stage of jet evolution is well known as a diffraction

phenomenon of a shock wave around a corner, which has been investigated for a long time by many researchers (Abe & Takayama 1990; Skews 1966, 1967; Takayama & Sekiguchi 1981). These studies were concerned with jets formed behind a shock which is produced in a shock tube and/or a reactive or explosive chamber.

The first shock, which passes through the open end of the tube or orifice, begins to diffract round the corner. In the next stage, a second shock which is generated in the vortex near the nozzle lip tends to spread toward the jet axis and finally to form a curved shock with an arc shape and an unsteady Mach disk (Abe & Takayama 1990; Yang & Takayama 1997). In the third stage, the first shock-cell structure is constructed, and for a strong jet a slip surface is generated downstream of the Mach disk. This surface produces Kelvin–Helmholtz instability waves and is responsible for generating the second vortices. In the final stage, a quasi-steady shock cell is formed near the open end and it begins self-sustained oscillation, radiating very strong pressure waves called 'screech' (Powell, Umeda & Ishii 1992; Umeda, Maeda & Ishii 1987; Umeda & Ishii 1993).

Although these phenomena are very interesting in a physical sense, so far the detailed flow characteristics of the jet in the second, third and final stages have not been made clear either experimentally or theoretically. So we believe that it is interesting and important to investigate systematically pulse jets for a wide range of jet strength.

In the present paper, unsteady circular jets are treated experimentally and numerically. Air is accelerated by a shock in a shock tube with a constant circular cross-section and exhausted from the open end into a test chamber. The jet strength is controlled by one parameter p_4/p_1, where p_1 and p_4 are initial gas pressures in the low-pressure and high-pressure chambers, respectively. In this experiment, the pressure ratios were chosen in the range from 2.0 to 50 to visualize the jets with shadowgraph and schlieren optical methods. The basic flow characteristics of the unsteady jet are investigated systematically, with the focus on the jet evolution in the second and third stages. The Kelvin–Helmholtz instability and the generation of the second vortices are investigated in detail in relation to the formation process of a Mach disk. The origin of asymmetric behaviour of the jet is also investigated. The numerical results are compared with the experiments and good agreement is obtained between them.

2. Flow system

We consider a very simple flow system composed of a shock tube with an open end and a test chamber, as schematically shown in figure 1, where A is the high-pressure chamber, B the low-pressure chamber and C the test chamber. The initial gas pressure in chamber A is p_4 and in chambers B and C it is p_1. Since chamber B is connected to the test section C through the open end, the initial gas condition in C is the same as that in B. When a diaphragm at the location O between chambers A and B is ruptured, a shock wave is produced in chamber B and propagates toward the open end E. On arriving at the open end, the shock begins to diffract round the end corner in the test chamber C and the accelerated gas is exhausted into C to form an unsteady pulse jet. When the pressure ratio p_4/p_1 is large enough, the gas flow after the shock becomes supersonic in B relative to the experimental system. Then the exit flow conditions of the gas at E become constant. When p_4/p_1 is not sufficiently large, the gas flow in B after the shock is subsonic relative to the experimental system and expansion waves enter chamber B from the open end E. So the flow conditions

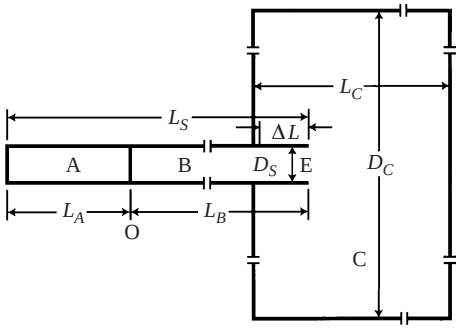

FIGURE 1. Flow field; $L_A = 40\,\text{cm}$, $L_B = 70\,\text{cm}$, $L_C = 36\,\text{cm}$, $D_S = 2\,\text{cm}$, $D_C = 32\,\text{cm}$.

at E change with time for a certain time interval. If the diameter D_C of the test section is sufficiently large compared with the duct diameter D_S, $D_C/D_S \gg 1$, the gas pressure at the duct lip will tend to recover its initial value after a certain time. A rough estimation will give a 'relaxation time' $\Delta t_E \sim O(D_C/c_1)$ for the pressure at E to recover its initial value p_1, where c_1 is the sound velocity of the gas in C.

3. Shock tube flow

In the numerical analysis, flows both in the shock tube and the test section must be solved simultaneously. To understand the basic characteristics of the present flow system, however, it is convenient to divide the whole flow region into two parts: a confined flow region in the shock tube and a free flow region in the test section.

The gas flow field in the shock tube will be almost one-dimensional, except for a short region $\Delta L \sim D_S$ near the open end. Since we can assume that $D_S/D_C \ll 1$ and $\Delta L/L_B \ll 1$ in the present study (where L_B is the length of the low-pressure chamber, see figure 1), the flow in the shock tube can be regarded as nearly one-dimensional. In this case, we can estimate systematically the gas flow exhausting from the open end E to the test chamber. In the one-dimensional approximation, it is assumed that the gas pressure at the nozzle lip at the open end is always constant, $p = p_1$. Theoretically, we have three types of constant flow conditions for some time interval ΔT at the open end as schematically shown in figure 2, where t is the time and x is the axial distance along the shock tube. This time interval ΔT is defined as the interval between the arrival time of the shock and that of the contact surface at E.

In order to make the discussion more quantitative, the following Rankine–Hugoniot relations across a moving shock are used:

$$\frac{p_2}{p_1} = 1 + \frac{2\gamma}{\gamma+1}(M^2 - 1), \tag{1}$$

$$\frac{\rho_2}{\rho_1} = \frac{(\gamma+1)M^2}{2 + (\gamma-1)M^2}, \tag{2}$$

$$u_2 = \frac{2c_1}{\gamma+1}\left(M - \frac{1}{M}\right), \tag{3}$$

where

$$M = U_s/c_1, \tag{4}$$

$$c_1^2 = \gamma p_1/\rho_1. \tag{5}$$

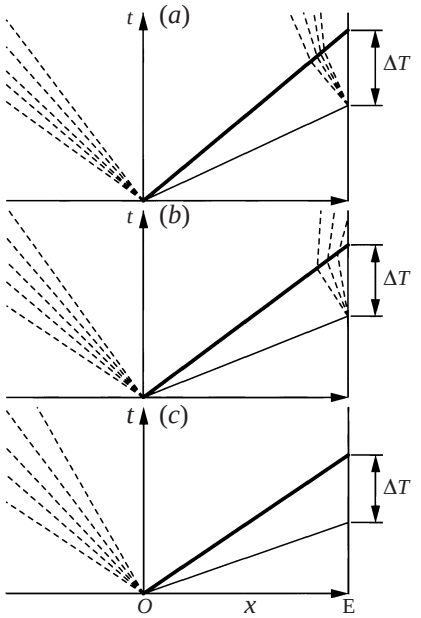

FIGURE 2. x, t diagrams of the density distribution in a one-dimensional shock tube for three different conditions as described in the text.

Here U_s is the shock velocity, c is the sound velocity, M is the shock Mach number, u is the gas velocity in the coordinate system fixed on the shock tube and γ is the ratio of specific heats of the gas. The subscripts 1 and 4 denote the initial gas conditions in chambers A and B, respectively, and the subscript 2 denotes the gas condition just behind the shock front. As a solution of a Riemann problem, the shock Mach number M can be given in terms of the initial pressure ratio p_4/p_1 as

$$\frac{p_4}{p_1} = \left[\frac{2\gamma M^2 - (\gamma - 1)}{\gamma + 1}\right] \Bigg/ \left[1 - \frac{\gamma - 1}{\gamma + 1}\left(M - \frac{1}{M}\right)\right]^{2\gamma/(\gamma-1)}. \tag{6}$$

Using this, equation (3) yields

$$M_2 = u_2/c_2 = 1.0 \quad \text{for} \quad p_4/p_1 = 41.2$$

for $\gamma = 7/5$. So the flow at E is supersonic relative to the experimental system for $p_4/p_1 > 41.2$ and then the flow conditions here are given by (M_2, ρ_2, p_2). For p_4/p_1 less than 41.2, M_2 is less than unity and expansion waves enter the duct from E after passage of the shock. In this case the gas condition at E is related to that just behind the shock by

$$u_E + \frac{2c_E}{\gamma - 1} = u_2 + \frac{2c_2}{\gamma - 1}, \tag{7}$$

$$\frac{p_E}{p_2} = \left(\frac{\rho_E}{\rho_2}\right)^{\gamma}, \tag{8}$$

where the subscript E denotes the gas conditions at E. Here it was assumed that the

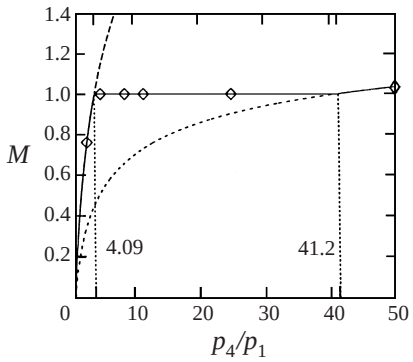

FIGURE 3. Mach number at the open end of the tube: ——, M_E; - - - -, M_2; - - -, M_{EI}; ◇, numerical results at $t = 200\,\mu s$ for the corresponding p_4/p_1 for the axially symmetric flow described in § 6.2.

gas is accelerated isentropically. Substituting $p_E = p_1$ into equations (7) and (8) yields

$$\left[\frac{2+(\gamma-1)M_2}{2+(\gamma-1)M_{EI}}\right]^{2\gamma/(\gamma-1)} = \frac{p_1}{p_2}, \tag{9}$$

where

$$M_{EI} = u_E/c_E. \tag{10}$$

For a specified pressure ratio p_4/p_1, equation (9) in conjunction with (1), (3) and (6) yields the exit Mach number M_{EI}. The numerical calculation shows that M_{EI} becomes unity for $p_4/p_1 = 4.1$, so the gas could be accelerated isentropically to a supersonic flow at E for a pressure ratio greater than 4.1. Practically, however, it is reasonable to expect that the choking phenomenon occurs at the end point E because $p_2 > p_1$, that is, the flow is just sonic at E for $4.1 < p_4/p_1 < 41.2$.

Summarizing these results, we can conclude that the flow conditions at E are

$$(a)\quad M_E = \left[M_2 + \frac{2}{(\gamma-1)}\right]\left(\frac{p_2}{p_1}\right)^{(\gamma-1)/2\gamma} - \frac{2}{(\gamma-1)}, \quad p_E = p_1, \quad \rho_E = \rho_2\left(\frac{p_2}{p_1}\right)^{-1/\gamma}$$

for $1 < p_4/p_1 < 4.1$, where the subscript E denotes flow condition realized asymptotically at a large time at the open end E;

$$(b)\quad M_E = 1, \quad p_E = p_2\left[\frac{2+(\gamma-1)M_2}{2+(\gamma-1)}\right]^{2\gamma/(\gamma-1)}, \quad \rho_E = \rho_2\left(\frac{p_2}{p_E}\right)^{-1/\gamma}$$

for $4.1 < p_4/p_1 < 41.2$;

$$(c)\quad M_E = M_2, \quad p_E = p_2, \quad \rho_E = \rho_2$$

for $41.2 < p_4/p_1$.

These three types of exit conditions are shown schematically in figures 2(*a*) to 2(*c*). The exit Mach number M_E is plotted against the initial pressure ratio p_4/p_1 by a solid line in figure 3. The short-dashed line shows the Mach number M_2 just behind the incident shock and the long-dashed line shows the possible Mach number M_{EI} that the gas can attain if the gas behind the incident shock is expanded isentropically from p_2 to p_1. From this, we can conclude that the jets exhausted from the open end E tend to be subsonic matched jets for $1 < p_4/p_1 < 4.1$, sonic underexpanded jets for

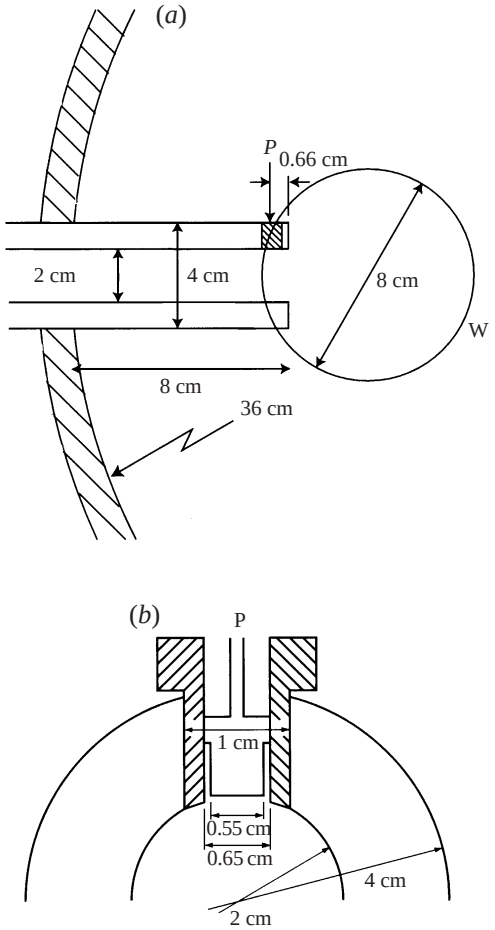

FIGURE 4. Dimensions of the test section: P is the piezo pressure transducer, and W the optical window. (*a*) Side view, (*b*) duct cross-section.

$4.1 < p_4/p_1 < 41.2$ and supersonic underexpanded jets for $41.2 < p_4/p_1$. Thus, we can realize three types of jets in the present system.

Actually, the flow field is not one-dimensional but axially symmetric, and so the flow properties have spatial distributions in the end plane. For example, the gas pressure p_j is not uniform in the radial direction at E, where p_j is the gas pressure after the jet blast, which will change from p_2 to p_E with increasing time.

4. Experiments

A conventional shock tube made of stainless steel was used and its dimensions are shown in figure 1. The detailed dimensions in the test section are shown in figure 4, where (*a*) is the side view and (*b*) is the duct cross-section through the centre of the piezo pressure transducer. The inner diameter of the shock tube is 2 cm and the piezo pressure transducer was mounted at a point P which is 6.6 mm from the open end E. Another transducer was set 20 cm upstream of point P. These were used to measure the shock velocity and the pressure changes at these points. The diaphragm was ruptured by a thin needle at a specified pressure ratio p_4/p_1. The arrival time of

p_4/p_1	$T_1 = T_4$ (K)	M_1	p_2/p_1	u_2/c_2	M_E	p_E/p_1
2.9	295	1.25	1.67	0.353	0.758	1.00
5.0	287	1.40	2.13	0.513	1.00	1.18
8.7	297	1.56	2.67	0.661	1.00	1.79
11.8	289	1.66	3.05	0.732	1.00	2.20
25.0	289	1.90	4.05	0.903	1.00	3.61
50.0	289	2.10	5.00	1.02	1.02	5.00

TABLE 1. Experimental conditions.

a shock at the open end E was calculated through the measured shock velocity and the distance between the points P and E.

The exhausted gas jets were visualized by a schlieren and/or shadow device with a spark light source of a duration of about 1 μs. The optical window has a diameter of 8 cm. A synchronized system enabled us to take instantaneous photographs at given instants. Several photographs were taken for a specified pressure ratio to confirm the reproducibility of the shock strength and the resultant jet flow. As will be shown later (figure 14), the main shocks produced in the test section were captured at a particular time instant with a scatter in the distances travelled from the open shock tube end of within 3%.

The pressure ratio p_4/p_1 was chosen as a control parameter of the jet. The experimental conditions are shown in table 1, where the temperatures T are those at which the experiments were performed. For these conditions, the possible times taken for the contact surface to reach the open end of the tube change from 800 μs to 1500 μs depending on the pressure ratio. This was confirmed both by the experiment and the numerical simulation. When the shock enters the test chamber, it is diffracted and proceeds in the outer direction as well as downstream. The time taken for the shock to be reflected at the chamber wall and to come back to the flow region that is confirmable through the optical window is more than 1000 μs, and so for the present experiment, jet evolutions were measured only for the first 500 μs to maintain good free jet conditions. The time zero is taken as the arrival time of the shock at the open end E. The Reynolds number based on the nozzle diameter is about 10^5.

5. Numerical simulation

For the theoretical interpretation of the experimental results, numerical simulations were performed on a supercomputer Fujitsu VP-2600 at the Data Processing Center of Kyoto University. The Euler equations for an axially symmetric flow were solved by a finite-difference TVD-scheme proposed by Chakravarthy & Osher (1985). The computational domain is shown in figure 5 and the mesh number is 600×400. On the outer boundary AH and the downstream boundary GH, the ambient gas condition is applied: $(p, \rho, u, v) = (p_1, \rho_1, 0, 0)$, where ρ is the gas density, u the axial velocity and v the radial velocity of the gas flow. On the solid walls AB, BC, CD, DE and the jet axis FG, the symmetric condition is applied. On the upstream boundary EF inside the shock tube, the shock condition $(p, \rho, u, v) = (p_2, \rho_2, u_2, 0)$ is applied, where the quantities denoted by the subscript 2 are obtained through the Rankine–Hugoniot relations for a specified shock Mach number M. Corresponding to the experiments, the length CD was set to be equal to the duct radius $EF(= \frac{1}{2}D_s)$.

In the numerical simulation, the boundary conditions are responsible for serious

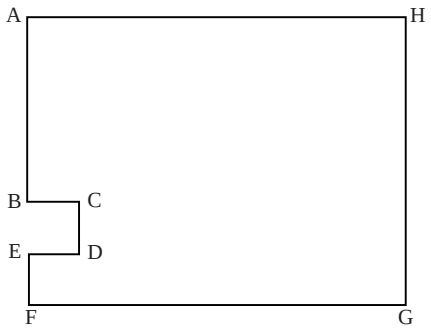

FIGURE 5. The computational domain.

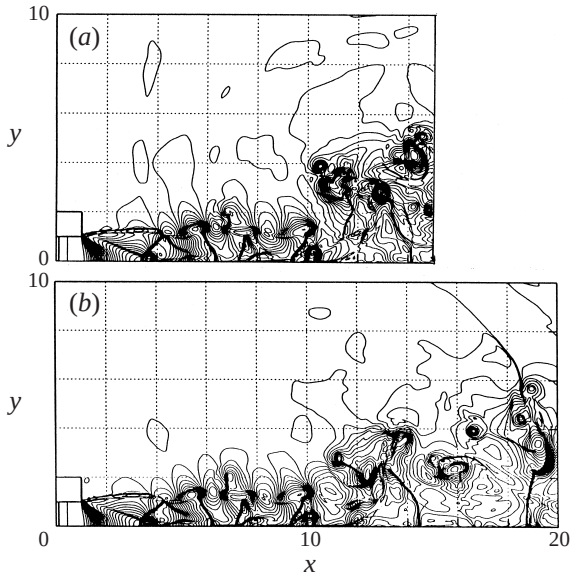

FIGURE 6. Density contours of a jet for $p_4/p_1 = 11.8$ at $t = 1140\,\mu s$.

artificial or unrealistic phenomena. This is because in the present case, the outer and downstream boundaries do not correspond to the actual boundaries. Empirically it is well known that the downstream boundary can affect the numerical results quite remarkably. Moreover, the flow inside the shock tube is not always supersonic and then the pressure waves may propagate into the shock tube. Numerically it was confirmed that the outer boundary does not affect the jet evolution appreciably if the length AB is taken as more than 5 times the size of the duct radius EF. So the total radius of the computational domain AF is taken to be $10 \times$ EF.

Here we first check the effect of the downstream boundary GH. Figure 6 shows the density contours of a jet for $p_4/p_1 = 11.8$ at $1140\,\mu s$, where x and y are the axial and radial coordinates, respectively, non-dimensionalized by the duct radius $\frac{1}{2}D_s = 1\,cm$ ($D_s = 2\,cm$). The non-dimensional mesh sizes $(\Delta x, \Delta y)$ are set as (0.05, 0.05). The only difference between jets (a) and (b) is the distance of the downstream boundary from the upstream one: 15 in case (a) and 20 in case (b). Obviously, both jet structures are almost the same for $0 \leqq x \leqq 10$ except for some weak pressure waves surrounding the jets. As confirmed previously, we can visualize and then investigate

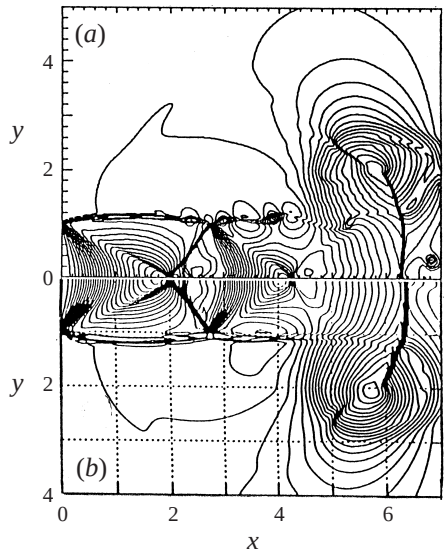

FIGURE 7. Density contours of a jet for $p_4/p_1 = 8.7$ at $t = 351\,\mu s$; (*a*) $(\Delta x, \Delta y) = (0.025,\ 0.025)$, (*b*) $(\Delta x, \Delta y) = (0.05,\ 0.05)$.

only the jets in a circular region with radius 4 cm whose centre is located at about $(x, y) = (4, 0)$. This suggests that the duct radius times 15 is quite sufficient as the axial length of the computational domain to reasonably investigate the jet evolution up to time 1000 μs in the numerical simulation. However, the effect of the downstream boundary was found to become significant with increasing computational time. It was also confirmed that an axial length equal to 10 times the size of the duct radius is enough to get reasonable numerical results in a time range of less than 500 μs.

Finally, we checked the effects of the mesh size on the computational results; a square mesh was used ($\Delta x = \Delta y$) throughout the present paper. It is generally well known that the numerical results depend on the mesh size, so it is important to see what kinds of phenomena we can predict with our mesh. Figures 7(*a*) and 7(*b*) show the density contours of a jet for $p_4/p_1 = 8.7$ at 351 μs; the only difference between the computational conditions is the mesh size Δx: set at 0.025 in (*a*) and 0.05 in (*b*). As we can see, the results agree quite well with each other and so, we can expect that strong phenomena such as the jet boundary, expansion waves, shock wave and strong vortical structure can be well predicted in the unsteady pulse jets. Only Kelvin–Helmholtz roll-up and the resultant fluctuations depend appreciably on the mesh size. In what follows, the mesh size $\Delta x = \Delta y = 0.025$ is taken as the reference. The present TVD-scheme can solve the one-dimensional shock tube problem with 99.9% accuracy, that is the numerical results predict the Rankine–Hugoniot relations within 0.1% error. A normal shock can be captured with 4 or 5 meshes.

6. Results and discussion

6.1. *Experimental results*

First, we investigated the time variation of the flow conditions that are realized at the open end E. Figure 8 shows the pressure change with time at the centre of the open end E for a pressure ratio $p_4/p_1 = 8.7$, obtained numerically. As might be expected, the pressure p_j changes from $p_2 = 2.67p_1$ to its asymptotic value $p_E = 1.79p_1$ almost

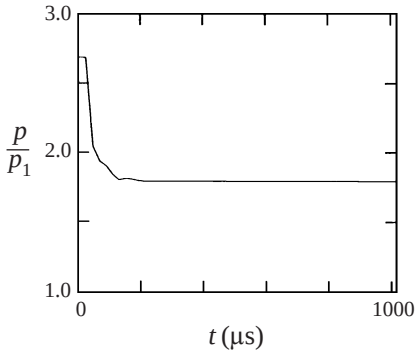

FIGURE 8. Time history of pressure at the duct centre for $p_4/p_1 = 8.7$.

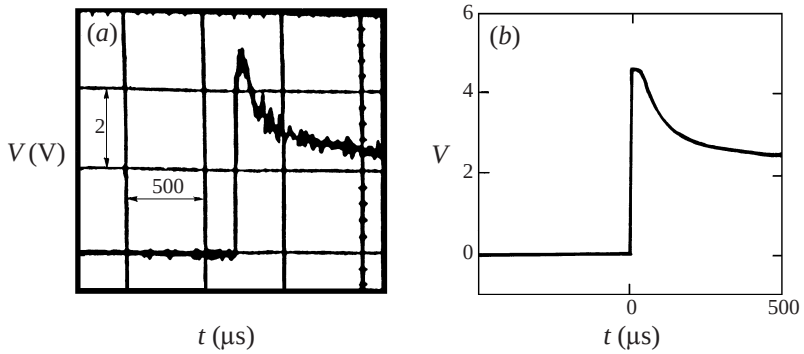

FIGURE 9. Comparison of time history measured by the piezo pressure transducer at point P (*a*) with the numerical result (*b*).

exponentially. About 100 μs is enough time for the pressure to reach a constant value. Figure 9 shows the time history of the pressure at a point on the wall located 6.6 mm upstream of the tube end E for $p_4/p_1 = 8.7$. Part (*a*) is the experimental result obtained by an oscilloscope with the piezo pressure transducer, and (*b*) is that obtained numerically. Since 1 V corresponds to 0.563 atm through the calibration, the results agree very well with each other, except for the high-frequency noise in the experiment. From these, it can be expected that the experimental flow phenomena at the open end will be well predicted theoretically.

In underexpanded sonic or supersonic pulse jets, shock waves as well as vortices are always produced. Figure 10(*a*) shows schematically a typical jet structure in the second stage. Here D_M, X_M and (X_V, Y_V) denote the diameter, the axial distance of the Mach disk and the location of the first vortex, respectively. Figures 10(*b*) and 10(*c*) show the jets at $t = 91$ and 181 μs, respectively, for $p_4/p_1 = 25$.

A series of photographs is shown in figures 11 to 13. The time zero is the arrival of first shock at the open end E. The jets in figure 11 are subsonic matched jets for $p_4/p_1 = 2.9$. A ring vortex is produced near the duct lip and its size increase with time during convection. Slip lines from the nozzle exit are clearly seen. Although some pressure waves and fluctuations are seen in the jets, no shocks are formed.

Underexpanded sonic jets for $p_4/p_1 = 5.0$ ($p_E/p_1 = 1.18$) are shown in figure 12. The second and the vortex-induced shocks are formed at $t = 136$ μs. It has been confirmed experimentally as well as numerically (Matsuda *et al.* 1987) that

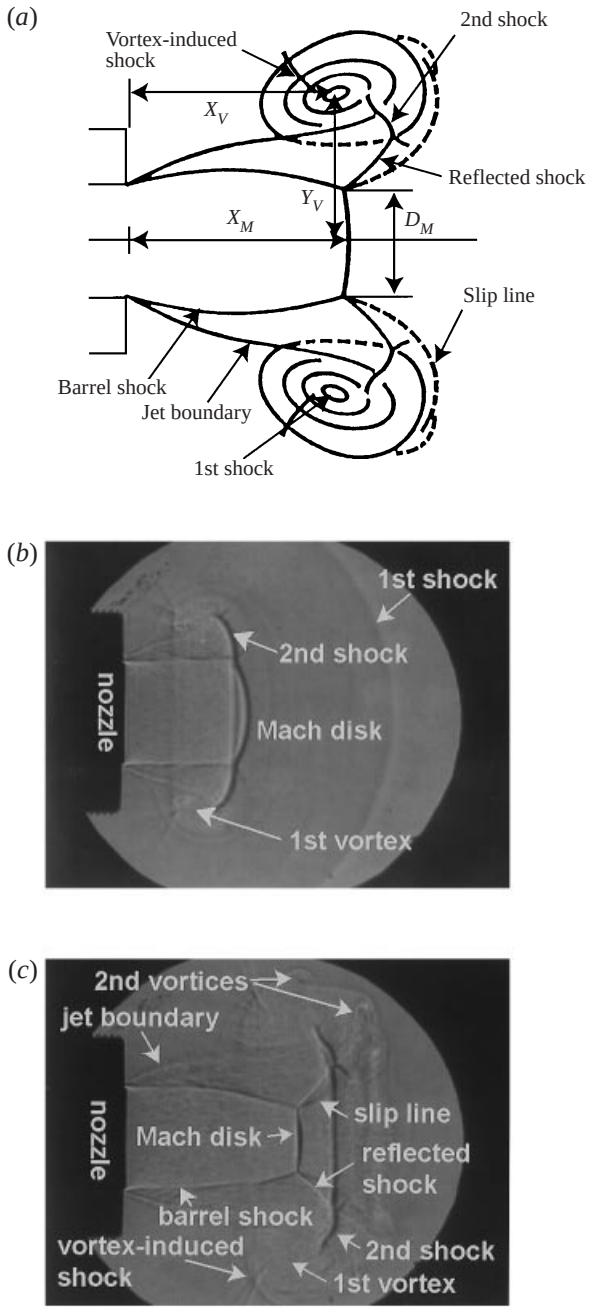

FIGURE 10. (*a*) Schematic view of the jet structure at the second stage, (*b*) jet structure at $t = 91\,\mu s$ for $p_4/p_1 = 25$, (*c*) jet structure at $t = 181\,\mu s$ for $p_4/p_1 = 25$.

the pressure ratio of the jet gas at the nozzle lip E to the ambient gas, p_j/p_1, is about 2.0 for the construction of a Mach disk in the quasi-steady jet. The pressure ratio p_j/p_1 for $p_4/p_1 = 5.0$ changes from 2.13 to 1.18 with increasing time. So there is a possibility that a Mach disk will be formed temporarily in this jet. Although something like a Mach disk is seen at $t = 136\,\mu s$ which disappears at $t = 156\,\mu s$, this

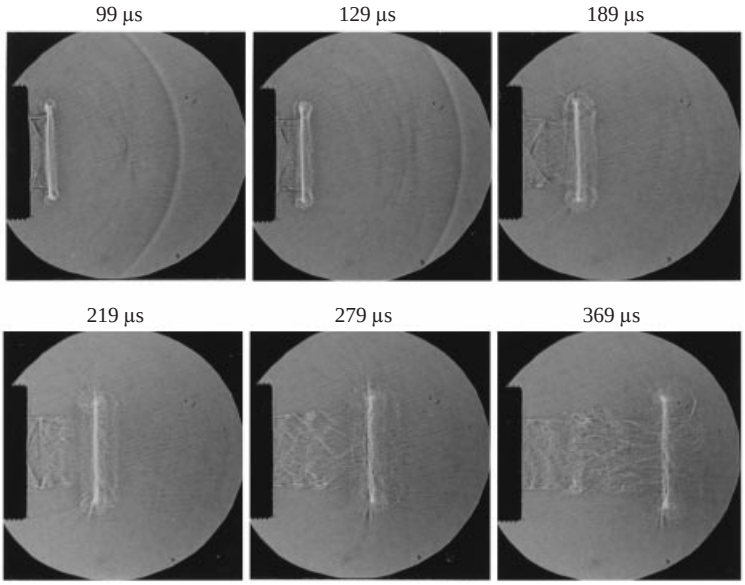

FIGURE 11. Time evolution of a pulse jet for $p_4/p_1 = 2.9$.

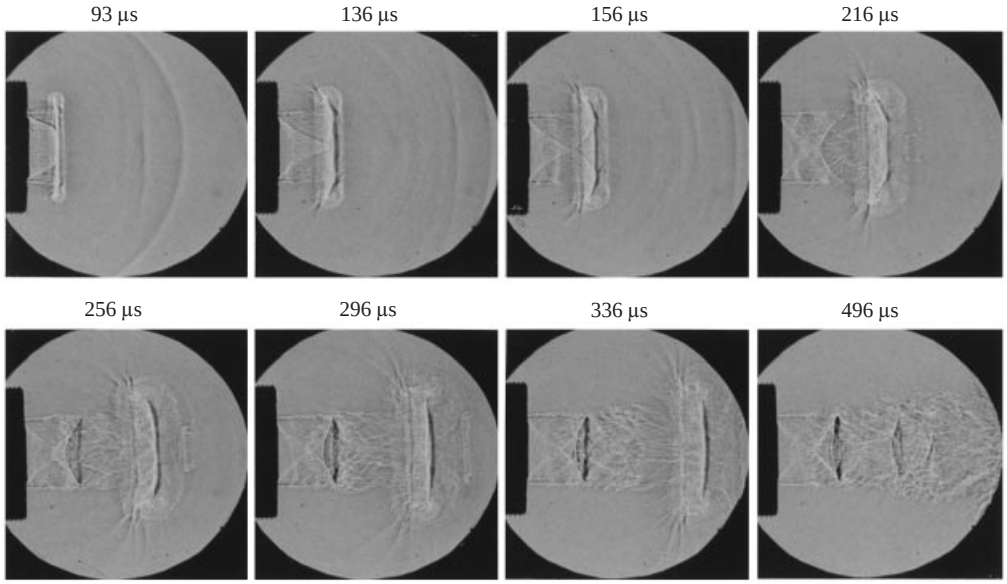

FIGURE 12. Time evolution of a pulse jet for $p_4/p_1 = 5.0$.

phenomenon is however weak shock interaction without a triple point. A reflected shock is connected to the second shock by this time, but the connection is broken by $t = 216\,\mu s$. Experimentally it is very difficult to distinguish a Mach disk from the reflected shocks at these times. In the jet at $t = 256\,\mu s$, even the reflected shocks cannot be seen clearly near the centreline.

It is interesting that the curvature of the reflected shock changes its sign rather abruptly during the evolution period from $t = 156$ to $216\,\mu s$. When the vortical

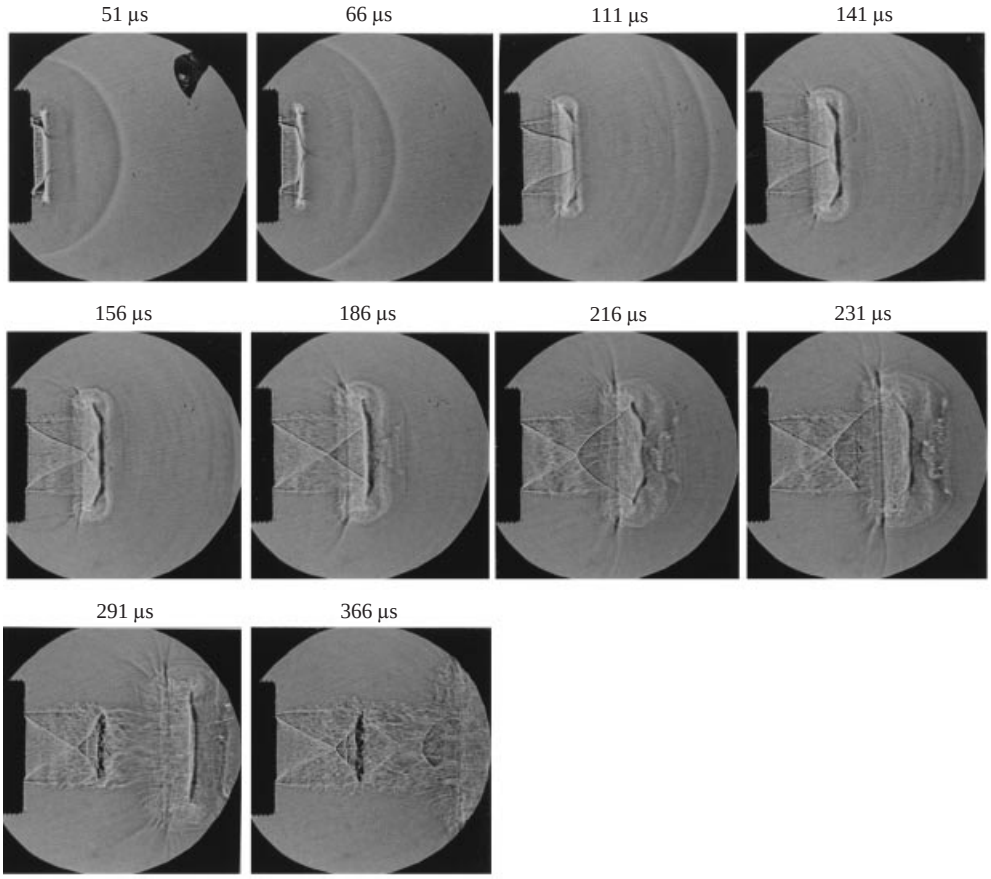

FIGURE 13. Time evolution of a pulse jet for $p_4/p_1 = 8.7$.

structure passes through the rear edge of the first shock cell, its axial length becomes largest. After this, it tends to shrink to some constant size. At $t = 256\,\mu s$, a new bow shock is seen a little downstream of the crossing point of the oblique shocks. This pair of shocks is called 'a double shock' and can be seen even in the quasi-steady jet (Raman 1998). It has been reported that this shock system is oscillatory with time (Panda 1998). In the jet at $t = 496\,\mu s$ we can see the second shock cell.

Sonic jets for $p_4/p_1 = 8.7$ ($p_E/p_1 = 1.79$) are shown in figure 13. The pressure ratio p_j/p_1 changes from 2.67 to 1.79 with increasing time. A Mach disk with a triple point has been formed by $t = 141\,\mu s$. The existence of the Mach disk formation can be confirmed by the presence of unsteady slip lines downstream of the triple points in the later jets, for example, at $t = 141$, 156 and 186 μs. This can also be simulated well numerically as shown later. The travelling normal shock is produced at about 231 μs just downstream of the crossing point of oblique shocks, and is convected downstream at a very low speed to form a double shock.

To discuss the phenomena more quantitatively, the motion of the incident (first) shock is plotted in figure 14. Obviously, its velocity depends on the jet strength near the open end, but after the jet blast it approaches asymptotically a sonic velocity. This means that it will take more than 1000 μs for the shock reflected from the downstream chamber wall to come back to the centre of the test section. This fact ensures the

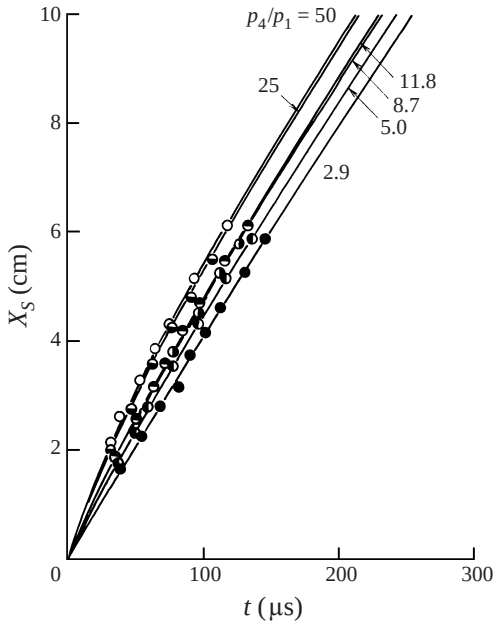

FIGURE 14. Motion of the incident (first) shock: ——, numerical; ○, $p_4/p_1 = 50$; ◒, $p_4/p_1 = 25$; ◓, $p_4/p_1 = 11.8$; ◑, $p_4/p_1 = 8.7$; ◐, $p_4/p_1 = 5.0$; ●, $p_4/p_1 = 2.9$.

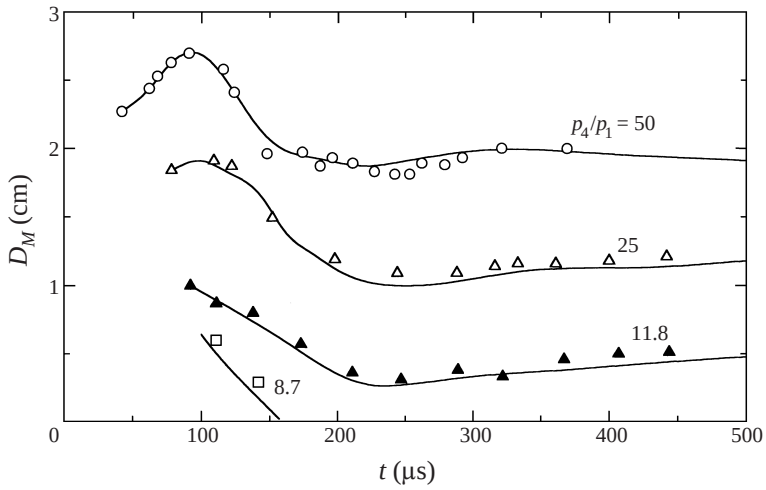

FIGURE 15. The diameter of the unsteady Mach disk: ——, numerical; ○, $p_4/p_1 = 50$; △, $p_4/p_1 = 25$; ▲, $p_4/p_1 = 11.8$; □, $p_4/p_1 = 8.7$.

free-jet condition for the flow field which can be observed from the optical window for $t < 1000\,\mu s$.

The motion of the Mach disk is shown in figures 15 and 16. For weak jets, the diameter D_M decreases after Mach disk formation, but it first increases to a maximum value and then decreases for strong jets. The diameter D_M of all jets with a quasi-steady Mach disk has a minimum value at about $250\,\mu s$.

The axial coordinate X_M increases quite monotonically after the disk formation but also has a maximum value at about $250\,\mu s$ and then decreases gradually to

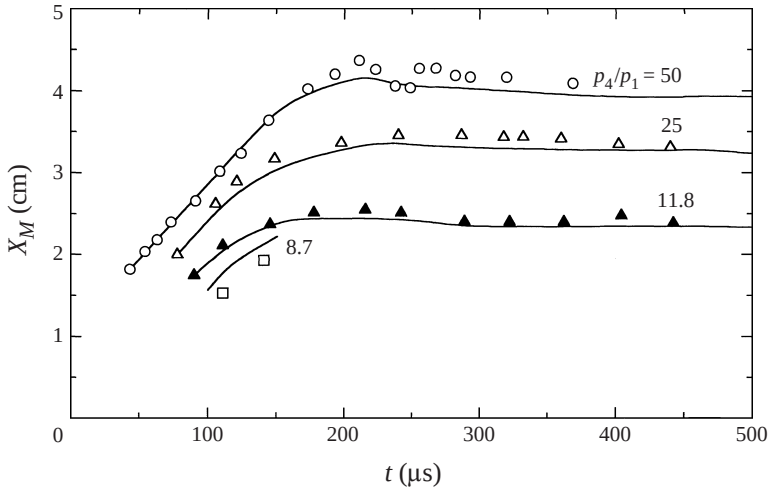

FIGURE 16. The axial distance of the unsteady Mach disk. Symbols as figure 15.

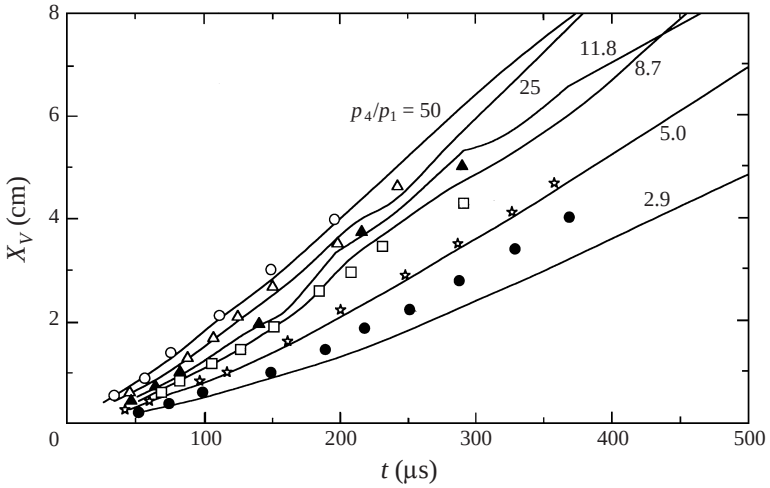

FIGURE 17. Axial coordinate of the first vortex: ——, numerical; ○, $p_4/p_1 = 50$; △, $p_4/p_1 = 25$; ▲, $p_4/p_1 = 11.8$; □, $p_4/p_1 = 8.7$; ☆, $p_4/p_1 = 5.0$; •, $p_4/p_1 = 2.9$.

some constant value. The Mach disk for $p_4/p_1 = 8.7$ is formed temporarily, but it disappears at about $t = 160\,\mu s$. At this moment, the axial coordinate is about 2.2 cm, as shown in figure 16.

For $p_4/p_1 = 50.0$, X_M fluctuates appreciably at $t = 200$–$240\,\mu s$. This phenomenon may be based on the convection of the second vortices around the first vortex. The second vortices tend to suppress the jet flow field in the radial direction and therefore cause the decrease in the diameter D_M. At $t = 440\,\mu s$, the diameters D_M are about 0.45 cm and 1.2 cm for $p_4/p_1 = 11.8$ and 25.0, respectively. These values are very close to the $D_M = 0.42$ cm and 1.3 cm for the corresponding quasi-steady sonic jets (Addy 1981; Matsuda *et al.* 1987).

The motion of the first vortex is shown in figures 17 and 18. As shown in figures 11 to 13, it is sometimes difficult to identify the vortex centre, especially for strong jets. With increasing time, pressure or density fluctuations become strong, especially

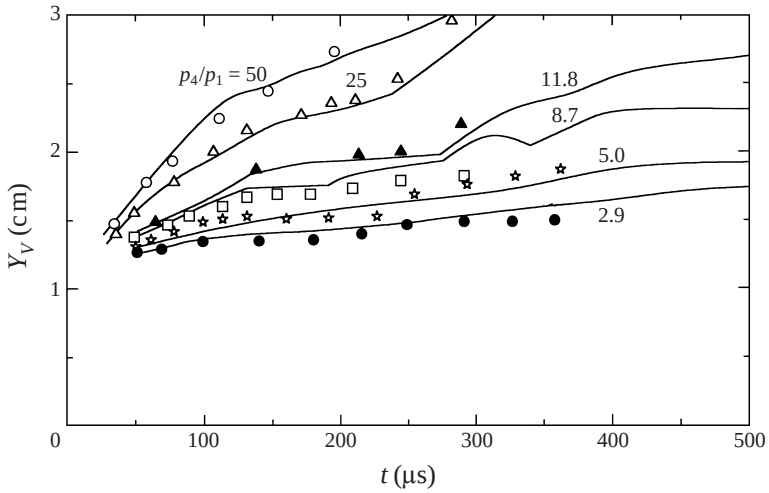

FIGURE 18. Radial distance of the first vortex. Symbols as figure 17.

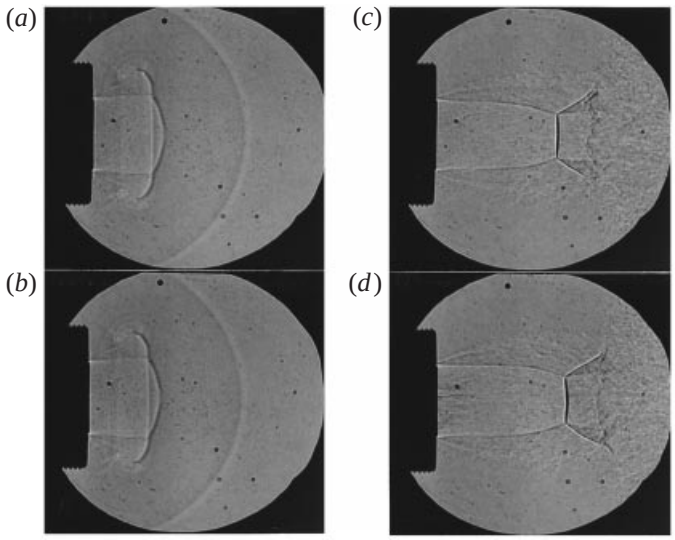

FIGURE 19. Reproducibility of experimental jets for $p_4/p_1 = 25$. For details, see the text.

near the vortex, and the vortex shape tends to be distorted appreciably. So 10%–20% scatter must be expected for the plotted data at least after 200 μs for jets with a Mach disk. Figure 17 shows that the convection of the first vortex in the axial direction, X_V, is always faster with the increasing jet strength for $p_4/p_1 \leqq 8.7$. For jets with a Mach disk, this is not always the case, which is perhaps caused by the recoiling of second vortices generated along the slip lines originating from the triple point. The change in the radial coordinate Y_V of the first vortex in figure 18 increases abruptly at about 250 μs for the jets with a Mach disk ($p_4/p_1 \geqq 12$). Unfortunately, the vortical centres of these jets could not be identified in the pictures owing to the strong fluctuations at times greater than 300 μs.

Finally, the reproducibility of the jet structure is investigated. Figure 19 shows the underexpanded sonic jets for $p_4/p_1 = 25$, where the two jets (*a*) and (*b*) are obtained

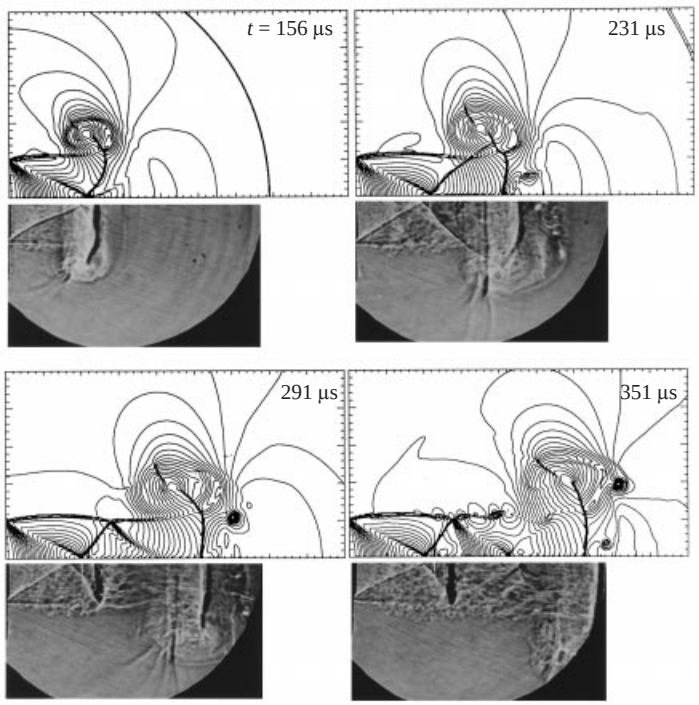

FIGURE 20. Comparison of experimental and numerical jets for $p_4/p_1 = 8.7$.

at $t = 61\,\mu s$ in different experimental runs, and (*c*) and (*d*) are from different runs at $t = 450\,\mu s$. No appreciable difference can be seen between the jet structures of (*a*) and (*b*), but the situation is different for (*c*) and (*d*). Where we can observe some differences in shape and size of the shock-cell structure. For example, the axial coordinate X_M of jet (*c*) is several percent shorter than that of (*d*), which suggests that the reproducibility becomes poorer with increasing observation time. Such a trend was confirmed for all the jets considered here. We can suggest three reasons for this. The first is the accuracy of the measurement of p_1 and p_4, and the second is the possible dependence of the flow on the rupture process of the diaphragm. Jets (*a*) and (*b*), however, suggest sufficient accuracy of the measurement pressures and a negligible dependence of the shock tube flow on the rupture process of the diaphragm. The third reason may be a physically important phenomenon. As discussed previously, the generation of the second vortices along the slip line is by the Kelvin–Helmholtz instability which is controlled by chaotic or unpredictable factors in the flow. These second vortices affect the fluctuations of the shock-cell structure and also the motion of the first vortex. This will result in appreciable scatter in the measured data for the shock-cell structure and the motion of the first vortex. Experimentally, therefore, each set of experimental data shown in the present paper were taken as ensemble averages over several photographs for a fixed pressure ratio at a specified instant.

6.2. *Numerical results*

Since the present numerical results are obtained with the Euler equations, the results will be particularly useful and meaningful for shock-dominant phenomena. The subsonic matched jet for $p_4/p_1 = 2.9$ shows no shock at all behind the first shock

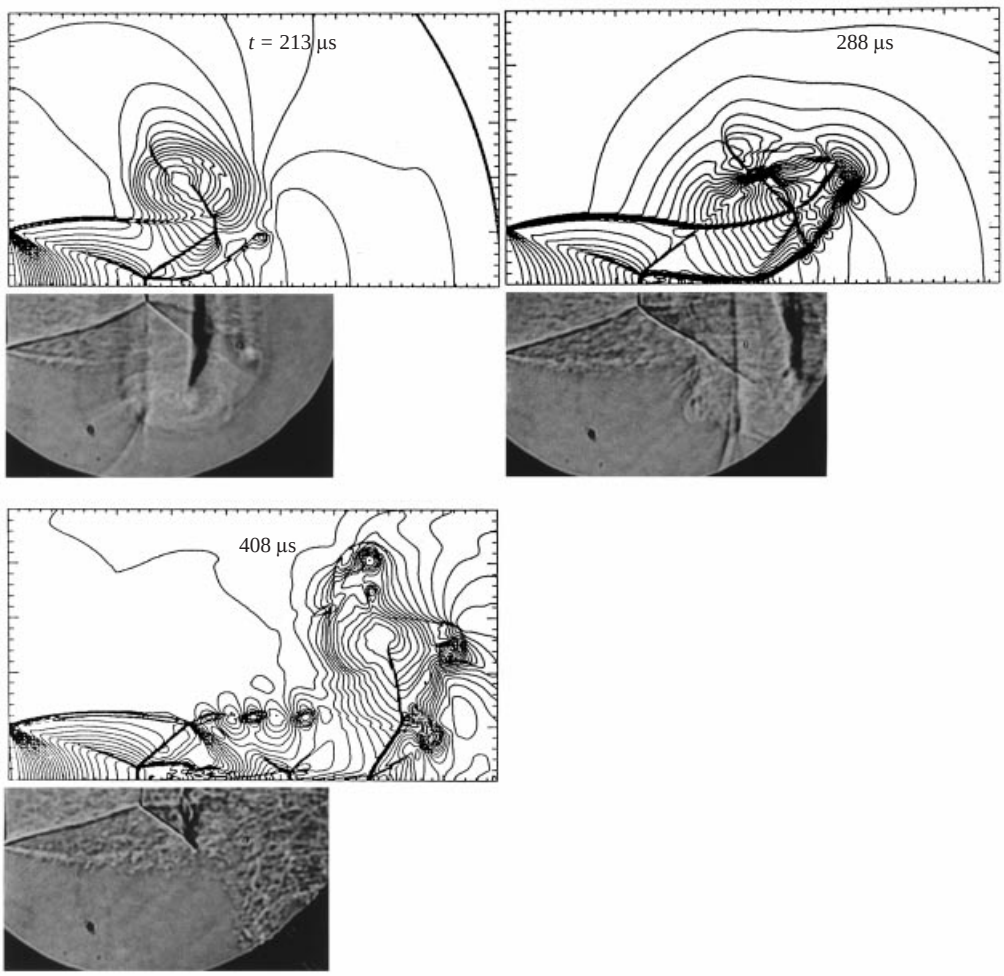

FIGURE 21. Comparison of experimental and numerical jets for $p_4/p_1 = 11.8$.

and so the time evolution of this jet will be controlled partly by the viscosity and the numerical results for this jet will become unrealistic with increasing time.

The motion of the incident (first) shock is shown in figure 14 for all jets considered here. Since the first shock is not affected appreciably by the subsequent jet evolution, the numerical results agree very well with the experiments.

Figures 20 to 22 show a comparison of density contours from numerical results with the corresponding photographs of the jets for $p_4/p_1 = 8.7, 11.8$ and 25, respectively. In figure 20, the jet at $t = 156\,\mu s$ shows the barrel and reflected shocks just after the decay of the unsteady Mach disk. It can be seen that a slip line originating from the crossing point of shocks is curved upward (see also figure 13). This represents the history of a decayed Mach disk. The centre of the first vortex is clearly seen in both the numerical and experimental jets. At $t = 231\,\mu s$, the first shock cell is elongated by the reflected shock connected to the second shock. At $t = 291\,\mu s$, the first shock-cell length shrinks by a few percent. The length of the numerical barrel shock is longer by about 25% than the experimental barrel shock. Agreement between the numerical and experimental jets is improved at $t = 351\,\mu s$.

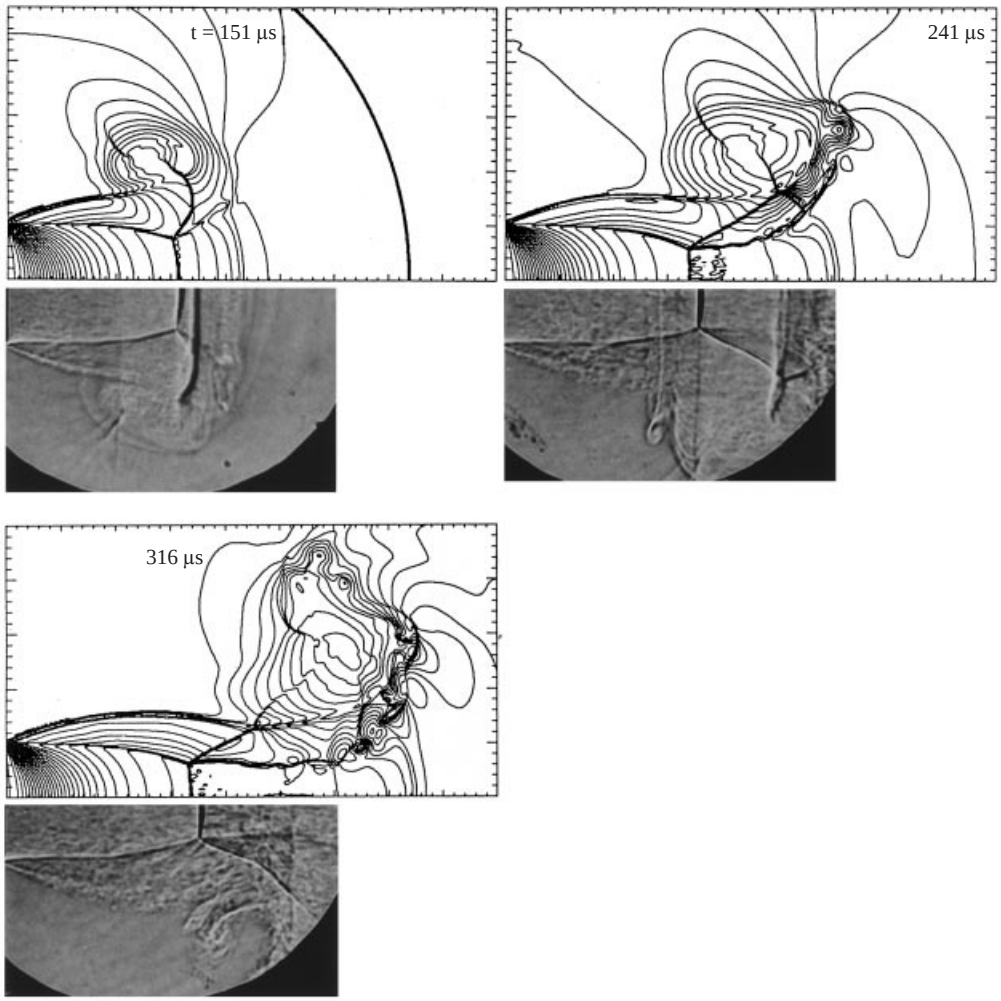

FIGURE 22. Comparison of experimental and numerical jets for $p_4/p_1 = 25.0$.

In order to investigate the unsteady Mach disk, numerical results for $p_4/p_1 = 8.7$ are shown in figure 24 where (*a*) and (*b*) show the density and the pressure contours, respectively, at $t = 110, 141$ and 166 μs. At about $t = 110$ μs, an unsteady Mach disk is formed. This is responsible for the appearance of unsteady slip lines in the jets at $t = 141$ and 166 μs, denoted by US. An appreciable difference in shape between the density and the pressure contours is seen downstream of the Mach disk in these jets, which means that the entropy changes across the unsteady slip lines. Such slip lines are seen at $t = 141$, 156 and 186 μs in the jets of figure 13.

In the numerical jets at $t = 231$, 291 and 351 μs in figure 20, we can see a few large second vortices. Although these vortices are also seen in the corresponding experimental jets, their sizes and numbers cannot be exactly estimated.

With increasing jet strength, the shocks produced in the jet become strong and the jet evolution becomes shock dominant. It is confirmed that the numerical jets predict very well the shock waves, slip lines and even the first vortices. Theoretically, the vortex motion will be affected appreciably by the gas viscosity. But the first vortex

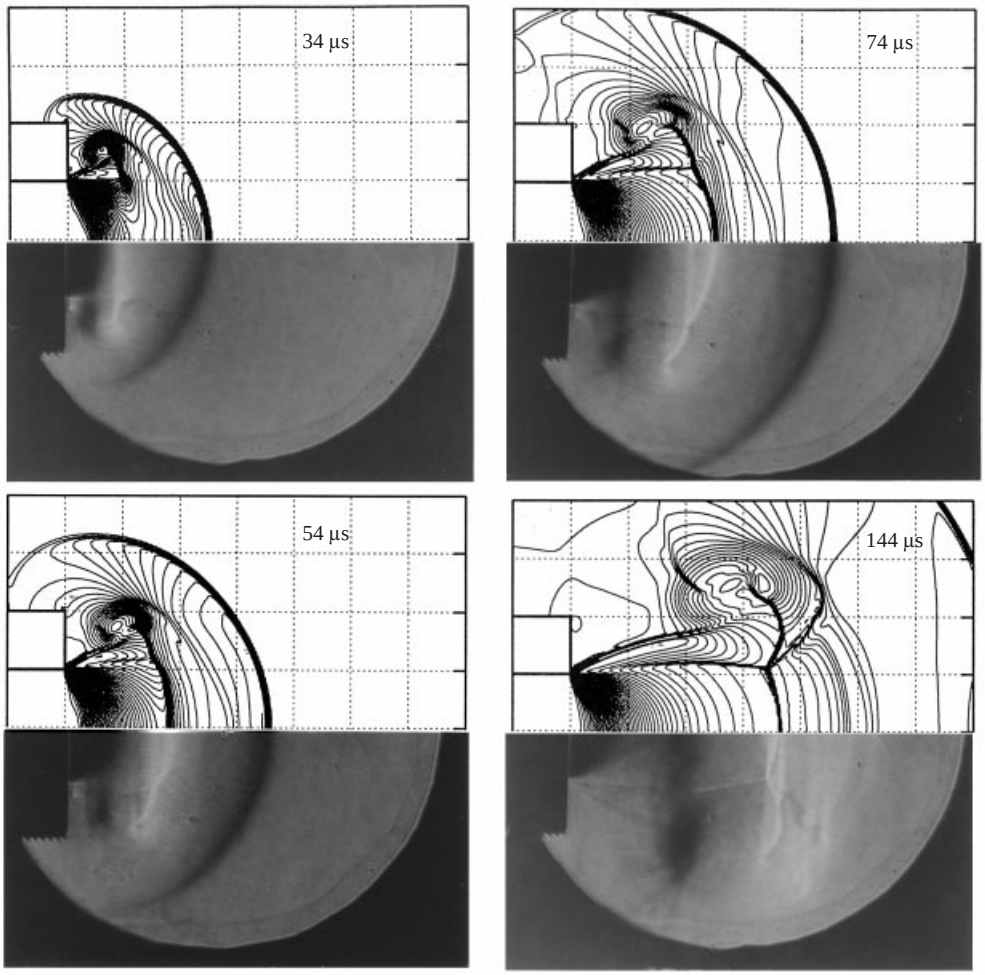

FIGURE 23. For caption see facing page.

contains the second and the vortex-induced shocks, both of which are strong and thus simulated well numerically. This may be why the viscosity-dominant phenomena (first vortices) can be simulated fairly well, at least in the early stage of jet evolution. In the numerical jet at $t = 231\,\mu s$, the second vortex is formed ahead of the second shock, which can also clearly be seen in the experimental jet.

The jets for $p_4/p_1 = 11.8$ shown in figure 21 have a few strong second vortices around the first vortex. Compared with the jets in figure 20, we can see that the numerical Kelvin–Helmholtz roll-ups along the jet boundaries are much more stronger. They are convected around the first vortex and even reach the upstream side of it. Experimentally these roll-ups are not seen well, perhaps owing to the strong fluctuations of three-dimensional structures. However the shocks and slip lines inside the jet are simulated very well, just as for the previous jets.

The jets shown in figure 22 have very strong Mach disks and the subsonic regions downstream of the Mach disks become much wider than those in the jets with $p_4/p_1 = 11.8$. The distance of the Mach disk from the tube, X_M, becomes a little

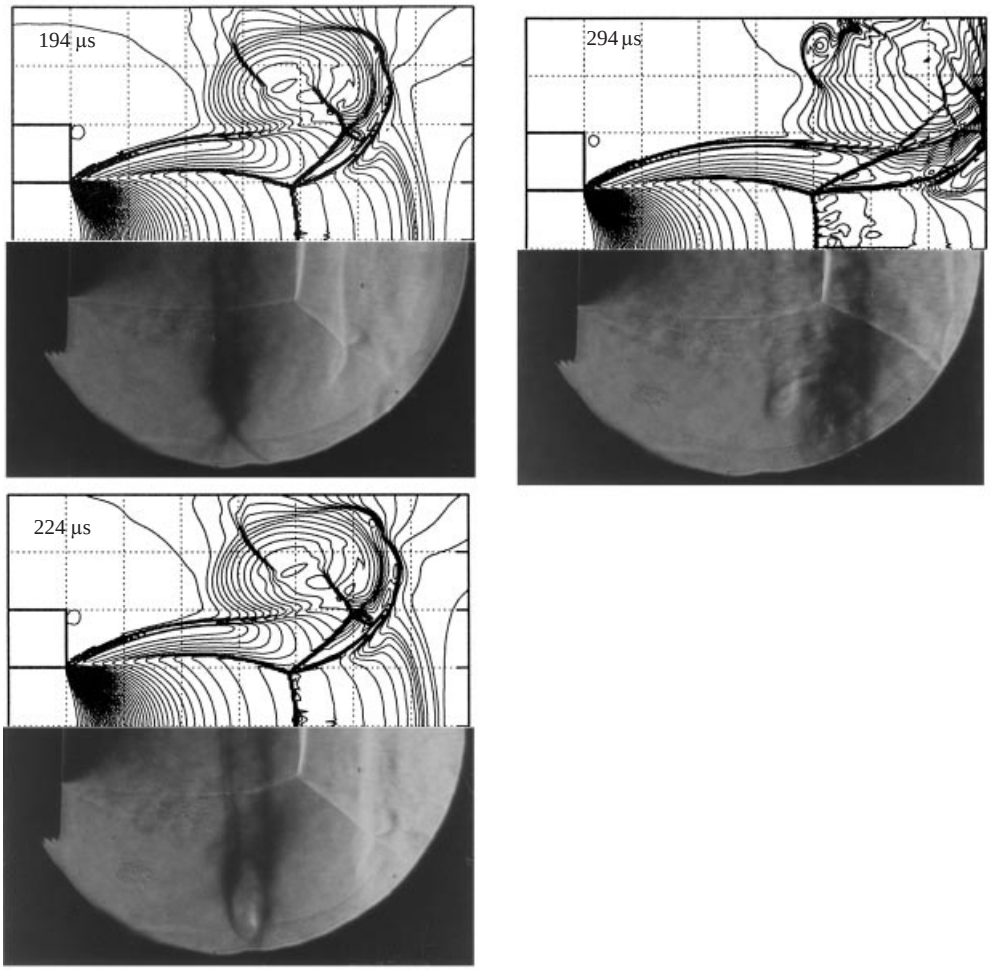

FIGURE 23. Comparison of experimental and numerical jets for $p_4/p_1 = 50.0$.

shorter than that of the experimental jets at $t = 241$ and 316 μs. The shock waves and the first vortices in the experimental jets, however, are simulated very well numerically.

Since the strong shock phenomena can be simulated very well, further comparisons between the numerical and the experimental results are made in figure 23 for the strongest jet ($p_4/p_1 = 50$) in the present study. In the jet at $t = 34$ μs, the first and the second shocks can be seen, but the Mach disk has not yet been formed. The Mach disk is formed at about $t = 54$ to 74 μs. Obviously its diameter is largest then and begins to shrink at about $t = 144$ μs. At this time instant, we can see a few Kelvin–Helmholtz roll-ups along the slip line. These second vortices seem to be affected appreciably by the gas viscosity and cannot be simulated well with the Euler equations. They are convected around the first vortex and so may restrict the motion of the first vortex.

Unfortunately the flow field that can be seen through the optical window is too narrow to observe these phenomena, so we can only predict them numerically. Although the simulated results, except for the shock-cell structure and the first vortex, only have qualitative meaning, phenomena such as the roll-ups, their growth,

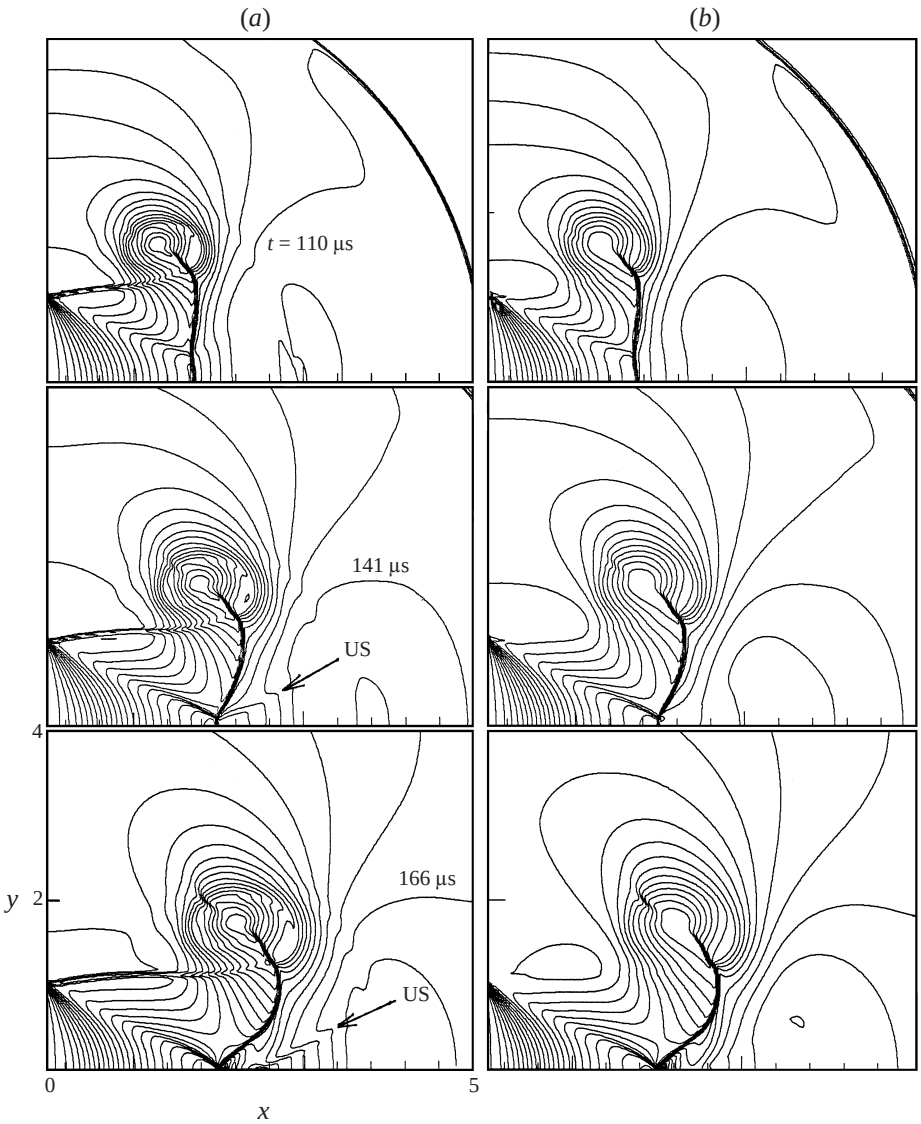

FIGURE 24. Numerical jets for $p_4/p_1 = 8.7$: (*a*) density and (*b*) pressure contours at three different times.

convection, the winding of the first vortex and break-up due to some complicated interactions in the flow field are clearly seen in the numerical simulation of figure 23. The simulated jet is unstable and rapidly breaks up. The jet tip is folded back on itself and is entrained into the vortex ring fed by the unstable shear layer emanating from the duct lip. Soon the jet evolves into a fully developed three-dimensional turbulent flow. Such phenomena cause effective mixing of the jet and the ambient gas (Kuhl *et al.* 1997).

Let us now investigate more systematically the characteristics of unsteady jets. The time change of the diameter D_M and the axial distance X_M of the Mach disks from the tube end are shown in figures 15 and 16, respectively. Good agreement between the numerical and experimental results has been obtained. The diameter D_M increases

p_4/p_1	t_{CE} μs (experimental) $t_{CE} = t_{CE}/(D_s/2c_1)$	t_{CN} μs (numerical) $t_{CN} = t_{CN}/(D_s/2c_1)$
5.0	180 ± 10 6.2 ± 0.3	175 ± 10 6.0 ± 0.3
8.7	200 ± 10 6.9 ± 0.3	200 ± 10 6.0 ± 0.3
11.8	240 ± 10 8.3 ± 0.3	240 ± 10 8.3 ± 0.3
25.0	280 ± 20 9.6 ± 0.7	260 ± 10 9.0 ± 0.3
50.0	280 ± 20 9.6 ± 0.7	260 ± 10 9.0 ± 0.3

TABLE 2. Time of formation of the first shock cell.

with time after disk formation for the strong jets ($p_4/p_1 = 25$ and 50), decreases to a minimum value and then tends to increase very gradually to some quasi-steady value. Here, it must be emphasized that we can never expect any completely steady free jet asymptotically. In quasi-steady screeching jets in a large anechoic chamber, supersonic jets always experience self-sustained oscillations called screech (Powell *et al.* 1992; Umeda & Ishii 1993). For the weaker jet ($p_4/p_1 = 11.8$), D_M decreases after disk formation and reaches a minimum at about $t = 250\,\mu s$ and then begins to increase. It is interesting that the jets for $p_4/p_1 = 11.8$, 25 and 50 reach their minimum diameters at nearly the same time, $t \sim 250\,\mu s$. It is also interesting that the jet for $p_4/p_1 = 8.7$ has an unsteady Mach disk temporarily but not a quasi-steady Mach disk. The axial distance X_M weakly overshoots at $t = 200$–$300\,\mu s$ and then tends to decrease slightly to some quasi-steady value.

Next the motions of the first vortices (X_V, Y_V) are plotted in figures 17 and 18, respectively. As discussed previously, identification of the vortical centre is very difficult experimentally. Agreement between the numerical and experimental results is rather poor in the later stages, particularly for the weakest and the strongest jets ($p_4/p_1 = 2.9$ and 50, respectively).

The second stage of jet evolution is difficult to investigate experimentally. The flow field is axially symmetric and the photographs show an integrated effect of the density distribution over the light path. So a normal shock with a hole or a ring-shaped shock appears as a Mach disk without any hole in the picture. But in the numerical jet, we can get density distributions on a plane through the jet axis and also detailed information in any local flow region. In the present study, we define the Mach disk as a single shock surface without the hole connected with barrel and reflected shocks. So the slip lines emanate from the triple points and the entropy changes across them.

It is rather arbitrary to define a time when the formation of the first shock cell is completed. Here the time is defined as that when the connection between the second shock and the reflected shock is broken. From the experimental and numerical results, we can get the construction time as in table 2. Both results agree fairly well and they show that the first shock cell is formed faster for the weaker jet.

Finally an important point must be checked. The present numerical simulations have been performed under the assumption that the jet evolution is axially symmetric. It is well known that the quasi-steady supersonic circular jet experiences self-sustained

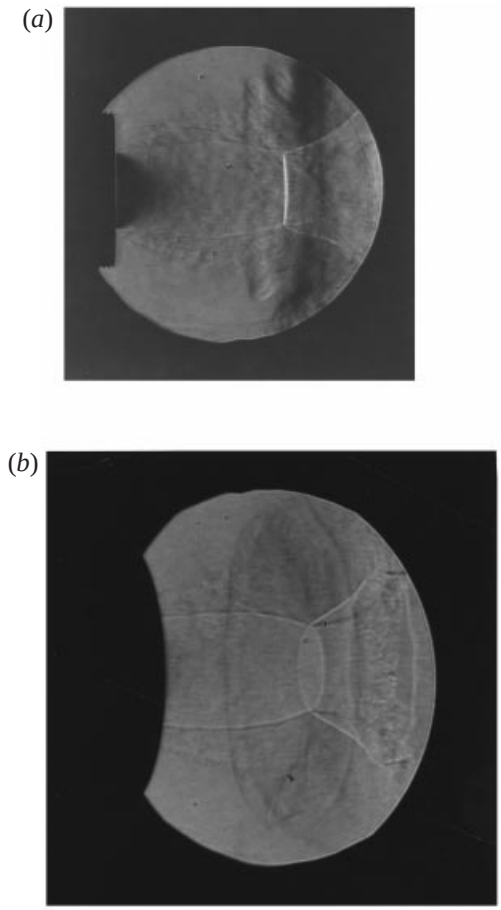

FIGURE 25. Structure of a strong jet for $p_4/p_1 = 50.0$ at $t = 244\,\mu s$: (*a*) along the jet axis, (*b*) at 60° to the jet axis.

oscillations. There are a few modes of oscillations which are not axially symmetric, which suggests the possibility that the axially symmetric numerical simulation is partly unrealistic. Figure 25 shows a jet for $p_4/p_1 = 50$ at $t = 244\,\mu s$. In (*a*), although the shock-cell structure is quite symmetric, the second vortices are not completely symmetric relative to the jet axis. To investigate the solid structure of this jet, a photograph is taken along a direction at 60° to the jet axis. Photograph (*b*) shows that the vortex-induced shock as well as the shock-cell structure are almost axially symmetric. The rear edge of the shock cell and the vortical structures deviate slightly from a circular shape. This suggests that it is reasonable to consider that the present numerical axisymmetric jets have predicted quite reasonably the experimental jets except for small-scale fluctuations.

7. Conclusions

Unsteady circular jets were investigated experimentally and numerically for a wide range of jet strength. After a sudden gas outflow, there are several stages in the subsequent time evolution of a sonic or supersonic underexpanded jet. The first stage is the diffraction of the first shock round the end corner. The second stage is the

formation of an unsteady Mach disk or a normal shock. Even in a jet which does not have a quasi-steady Mach disk, an unsteady Mach disk can be formed, at least temporarily. The third stage is the formation of the first shock-cell structure. This stage is strongly affected by the presence of the first vortex and the Mach disk. After the connection between the second shock and the reflected shock is broken, the shock-cell length becomes maximum and thereafter it tends to shrink to a certain asymptotic size. The jet with a strong Mach disk is very unstable and rapidly breaks up. The jet tip is folded back on itself and is entrained into the first vortex ring and the jet soon evolves to a fully developed turbulent flow. At least up to 500 μs, circular jets with 2 cm diameter experience a substantially axially symmetric time evolution.

It has also been confirmed that the numerical results obtained by a TVD-scheme for the Euler equations can successfully predict the formation process of the shock cell. In particular, the shock cell with a Mach disk is remarkably well simulated quantitatively as well as qualitatively. Unfortunately, the motion of the first vortex was not always well simulated quantitatively at large times, partly because the vortex motion is affected by the gas viscosity.

REFERENCES

Abe, A. & Takayama, K. 1990 Numerical simulation and density measurement of a shock wave discharge from the open end of a shock tube. *JSME Intl J.* II **33**, 246–223.

Addy, A. L. 1981 Effect of axisymmetric sonic nozzle geometry on Mach disk characteristics. *AIAA J.* **19**, 121–122.

Chakravarthy, S. R. & Osher, S. 1985 A new class of high accuracy TVD schemes for hyperbolic conservation laws. *AIAA Paper* 85-0363.

Elder, F. K. Jr. & De Haas, N. 1952 Experimental study of the formation of a vortex ring at the open end of a cylindrical shock tube. *J. Appl. Phys.* **23**, 1065–1069.

Golub, V. V. 1994 Development of shock wave and vortex structures in unsteady jets. *Shock Waves* **3**, 279–285.

Kuhl, A. L., Reinhenbach, H., Neuwald, P., Ferguson, R. E. & Oppenheim, A. K. 1997 Fluid mechanics of a planar exothermic jet. *JSME ICFE-97*, pp. 955–959.

Matsuda, T., Umeda, Y., Ishii, R., Yasuda, A. & Sawada, K. 1987 Numerical and experimental studies on choked underexpanded jets. *AIAA Paper* 87-1378.

Oppenheim, A. K. & Maxon, J. A. 1991 Thermodynamics of combusion in an enclosure, dynamics of heterogeneous combustion and reacting system. Progress in Astronautics and Aeronautics, vol. 1 (ed. A. L. Kuhl, J. G. Leyer, A. A. Borisov & W. A. Sirignano) pp. 251–261. *AIAA*.

Panda, J. 1998 Shock oscillation in underexpanded screeching jets. *J. Fluid Mech.* **363**, 173–198.

Payman, W. & Shepherd, W. C. F. 1946 Explosion and shock waves VI. The disturbance produced by bursting diaphragm with compressed air. *Proc. R. Soc. Lond.* A **186**, 293–321.

Powell, A., Umeda, Y. & Ishii, R. 1992 Observation of the oscillation modes of circular choked jets. *J. Acoust. Soc. Am.* **92**, 2823–2836.

Raman, G. 1998 Advances in underexpanding supersonic jet screech. *AIAA Paper* 98-0279.

Schmidt, E. M. & Shear, D. D. 1975 Optical measurements of muzzle blast. *AIAA J.* **13**, 1086–1091.

Skews, B. W. 1966 The shape of a diffraction of shock wave. *J. Fluid Mech.* **29**, 297–304.

Skews, B. W. 1967 The perturbed region behind a diffracting shock wave. *J. Fluid Mech.* **29**, 705–720.

Takayama, K. & Sekiguchi, H. 1981 Formation and diffraction of spherical shock waves in a shock tube. *Rep. Inst. High Speed Mech., Tohoku Univ.*, vol. 43, pp. 89–119.

Umeda, Y. & Ishii, R. 1993 Oscillation modes of underexpanded jets issuing from square and equilateral triangular nozzles. *J. Acoust. Soc. Am.* **95**, 1853–1857.

Umeda, Y., Maeda, H. & Ishii, R. 1987 Discrete tones generated by the impingement of a high-speed jet on a circular cylinder. *Phys. Fluids* **30**, 2380–2388.

Yang, J. M. & Takayama, K. 1997 Shock wave diffraction at a 90° convex corner – A Report of Recent Development. *JSME ICFE-97*, pp. 157–161.